

Infrared Small Target Detection via Low-Rank Tensor Completion With Top-Hat Regularization

Hu Zhu¹, Member, IEEE, Shiming Liu, Lizhen Deng¹, Member, IEEE, Yansheng Li¹,
and Fu Xiao¹, Member, IEEE

Abstract—Infrared small target detection technology is one of the key technologies in the field of computer vision. In recent years, several methods have been proposed for detecting small infrared targets. However, the existing methods are highly sensitive to challenging heterogeneous backgrounds, which are mainly due to: 1) infrared images containing mostly heavy clouds and chaotic sea backgrounds and 2) the inefficiency of utilizing the structural prior knowledge of the target. In this article, we propose a novel approach for infrared small target detection in order to take both the structural prior knowledge of the target and the self-correlation of the background into account. First, we construct a tensor model for the high-dimensional structural characteristics of multiframe infrared images. Second, inspired by the low-rank background and morphological operator, a novel method based on low-rank tensor completion with top-hat regularization is proposed, which integrates low-rank tensor completion and a ring top-hat regularization into our model. Third, a closed solution to the optimization algorithm is given to solve the proposed tensor model. Furthermore, the experimental results from seven real infrared sequences demonstrate the superiority of the proposed small target detection method. Compared with traditional baseline methods, the proposed method can not only achieve an improvement in the signal-to-clutter ratio gain and background suppression factor but also provide a more robust detection model in situations with low false-positive rates.

Index Terms—Low-rank tensor completion, multiframe infrared image, ring top-hat regularization, small target detection, structural prior knowledge.

I. INTRODUCTION

INFRARED small target detection is an important technology for signal processing. With the development of the top-hat filter [1], matrix completion [2], [3], and tensor

completion [4]–[6], the related technologies of infrared small target detection have been greatly improved and significantly advanced the detection of accuracy. Infrared small target detection technology is widely used in various fields, such as aerospace technology [1], remote sensing [7], [8], medical imaging [9], and target detection and tracking [10]. However, it is still a challenging problem, mainly due to: 1) the complex background with low signal-to-clutter ratio (SCR) caused by cluttered noise and 2) dim targets with long-imaging distances. Specifically, small infrared targets may be affected by thick cloud or sea–sky plane [11]–[13]. Infrared small target detection has been studied for decades, and various infrared small target detection methods have been proposed to handle these challenges [14].

Recently, many infrared small target detection methods have been proposed, such as the max-mean/max-median filter [15] and the top-hat filter [1]. However, these methods require prior knowledge of the background scene, which limits the industrial applicability of the method. To solve this issue, nonparametric regression [16] is introduced to estimate the background of the changes. Benefiting from the salient prior assumption between the target and background, it is noticeable that the local priors play a significant role in infrared small target detection. For example, by only comparing a pixel or a region with its neighbors one can detect the target well, i.e., local contrast method [7], weighted local difference measure (WLDM) [17], derivative entropy-based contrast measure [18], local adaptive contrast operation based on regularized feature reconstruction [19], directional saliency-based method (DSBM) [20], multiscale patch-based contrast measure [21], and so on. Due to the strong edges and other interfering components in the image, the methods based on local differences may have a higher false alarm rate. To solve this challenge, a series of fuzzy metric methods are proposed, such as the multiscale fuzzy metric [22], multichannel kernel fuzzy correlogram [23], and an improved fuzzy c-means [24] method based on spatial information.

Low-rank matrix recovery has been studied for many years and applied to various fields. The inherent spatial correlation between the pixels of an image indicates that the background is expressed in a continuous way, and the pixels are highly correlated. In contrast, the target is viewed as the object that breaks this local correlation. Therefore, the segmentation of the target from the background can be seen as the recovery of the low-rank matrix. However, rank minimization is an NP-hard

Manuscript received April 21, 2019; revised August 10, 2019; accepted September 6, 2019. This work was supported by the National Natural Science Foundation under Grant 61701259, Grant 61671253, and Grant 41601352. (Corresponding author: Lizhen Deng.)

H. Zhu and S. Liu are with the Jiangsu Province Key Laboratory on Image Processing and Image Communication, Nanjing University of Posts and Telecommunications, Nanjing 210003, China (e-mail: peter.hu.zhu@gmail.com; never66liu@163.com).

L. Deng is with the National Engineering Research Center of Communication and Network Technology, Nanjing University of Posts and Telecommunications, Nanjing 210003, China (e-mail: alicedenglzh@gmail.com).

Y. Li is with the School of Remote Sensing and Information Engineering, Wuhan University, Wuhan 430079, China (e-mail: liyansheng99@gmail.com).

F. Xiao is with the Jiangsu High Technology Research Key Laboratory for Wireless Sensor Networks, Nanjing University of Posts and Telecommunications, Nanjing 210023, China (e-mail: xiaof@njupt.edu.cn).

Color versions of one or more of the figures in this article are available online at <http://ieeexplore.ieee.org>.

Digital Object Identifier 10.1109/TGRS.2019.2942384

problem. To solve this challenge, the nuclear norm [25], [26] is often used as an alternative to the rank function. Gao *et al.* [2] proposed an infrared patch image model (IPM) based on the local block structure similarity, which described infrared small target detection as the optimization problem of restoring a low-rank and sparse matrix. To correctly detect infrared small targets located in highly heterogeneous backgrounds, He *et al.* [3] proposed a low-rank and sparse representation model under the multisubspace cluster hypothesis. However, nuclear norm minimization (NNM) tends to over shrink the rank components. Specifically, an approximation method is proposed in [27], which enforces low-rank regularization by using the Schatten p -norm, which is defined as the L_p norm of the singular values $(\sum_k \sigma_k^p(I_B))^{1/p}$ with $1 > p > 0$. However, the Schatten p -norm is not flexible enough to deal with different important rank components because it treats all singular values equally. Therefore, it has been proposed in [28] to solve the challenge by utilizing the Schatten p -norm. Since the detection of an infrared small target in a single-frame image only considers the low-rank structure in one unfolding, it lacks the main structural information, and it is not sufficient to handle a complex scene. Therefore, it motivates us to consider whether we can use the other two unfolding modes. In recent years, this idea of a low-rank constraint has been applied to the low-rank completion of tensors. Unlike a matrix, a tensor is a multilinear generation of a multidimensional matrix that usually directly operates on higher order data. In addition, this idea facilitates the learning process in which CANDECOMP/PARAFAC (CP), Tucker decomposition, or tensor train decomposition [29] and low-rank constraints in different mode expansion matrices are used, such as reweighted infrared patch tensor (RIPT) model [6]. Dai and Wu [6] proposed a target detection model based on nonlocal self-correlation ship and local tensor structure priors. In addition, a local prior is added for optimizing the problem of nonlocal low-rank tensor recovery. While Dai and Wu [6] exploited the NNM to reserve the constraints on the low-rank tensor, this algorithm ignored the importance of dissimilarities between different low-rank components. Low-rank tensor constraints have been applied in different fields, such as Tucker decomposition for discriminative tracking [30], big data driven [31], hyperspectral image denoising [32], tensor completion for estimating missing values [4], and low-rank tensor train [5].

Mathematical morphology is a theory and technique for the analysis and processing of geometrical structures of image [33]. In recent years, morphology has been widely used in infrared small target detection. Bin and Xiong [34] proposed a method-based top-hat operator for small target detection. However, the traditional morphological operator uses a uniform structuring element, which ignored the information between the target and the surrounding area and resulted in an unsatisfactory detection effect. A new morphological operator [35], [36] with two different structuring elements was proposed to solve this shortcoming. The shape and pixel values of the structuring elements are important factors for the final result of the morphological target detection. However, the prior knowledge of structuring elements is not

known, and the selection of structural elements is a hard task. Recently, the combination of morphology and neural networks has become a major trend, such as the use of neural networks and genetic algorithms to extract the structuring element information of the morphology [1], suppression neural network [37], and morphological sharing weight network [38]. However, a large amount of training data is required, and the calculation is expensive.

In this article, in order to solve the problem of different low-rank components with different importance and insufficient local prior knowledge, we propose a novel infrared target detection method based on low-rank tensor completion with top-hat regularization (TCTHR). We have listed the main contributions of this article as follows.

- 1) We propose that the traditional top-hat transformation is tailored into top-hat regularization term for addressing infrared small target detection for the sake of penalizing the noises and clutters. In addition, ring top-hat regularization term is formulated into our proposed detection model to properly utilize the local structural prior to the target and antinoise.
- 2) To properly enforce the low-rank regularization for different low-rank components of tensor data, we introduce a weighted Schatten p -norm into the tensor model, which makes the most use of the structural characteristics of the low-rank tensor.
- 3) We propose a novel infrared small target detection tensor model (TCTHR) and introduce the detailed solution process of the alternating direction multiplier method (ADMM).

This article is organized as follows. In Section II, we introduce in detail the theoretical basis of our model, the proposed model, and the related solution process. In Section III, we give some preliminaries for tensor and tensor decomposition, and the background of morphological regularization. In Section IV, we conducted many experiments and verified the superiority of our model from various aspects. In Section V, our conclusion is given.

II. PRELIMINARIES

A. Tensor Notation and K -Mode Unfolding

In this article, we use lower case letters to denote vectors, e.g., t , upper case letters for matrices, e.g., $I_D, I_B \dots$, and calligraphic letters for tensors, e.g., $\mathcal{I}_D, \mathcal{I}_B \dots$. For a tensor of order N is denoted as $\mathcal{I}_D \in R^{I_1 \times I_2 \times \dots \times I_N}$. The elements of \mathcal{I}_D are denoted as $i_{d_1} \dots i_{d_n} \dots i_{d_N}$, where $1 \leq d_n \leq I_n$. For tensor $\mathcal{I}_D, \mathcal{I}_B \in R^{I_1 \times I_2 \times \dots \times I_N}$, we define the inner product as $\langle \mathcal{I}_D, \mathcal{I}_B \rangle = \sum_{i_1=1}^{I_1} \dots \sum_{i_N=1}^{I_N} i_{d(i_1 \dots i_N)} i_{b(i_1 \dots i_N)}$. The Frobenius norm of \mathcal{I}_D is defined as $\|\mathcal{I}_D\|_F = ((\mathcal{I}_D \cdot \mathcal{I}_D))^{1/2}$.

The mode- n unfolding matrix $I_{D(n)}$ obtained from \mathcal{I}_D is the process of unfolding or reshaping the tensor into a matrix by rearranging the mode- n fibers to be the columns of the resulting matrix. The unfolding matrix $I_{D(n)} = \text{unfold}_n(\mathcal{I}_D)$ is composed by taking the mode- n vectors of \mathcal{I}_D as its columns. At the same time, the mode- n unfolding matrix $I_{D(n)}$ of the tensor \mathcal{I}_D can also be transformed back to the tensor by $\mathcal{I}_D = \text{fold}_n(I_{D(n)})$, $1 \leq n \leq N$.

B. Background of Morphological Regularization

Morphological detection is the main research method for infrared small target detection, which mainly includes two basic operations: corrosion and expansion. In the infrared small target detection based on a morphological operator, the key technology is the design of the morphological operator and the structuring elements. At present, the top-hat operation has become a popular method for infrared small target detection.

We need to understand the structuring element and image information to be processed. Let b and f represent the structuring element and the image to be processed, respectively. The dilation and erosion of $f(x, y)$ by $b(u, v)$, denoted by $f \oplus b$ and $f \ominus b$, are defined by

$$(f \oplus b)(x, y) = \max_{u,v} (f(x-u), y-v) + b(u, v) \quad (1)$$

$$(f \ominus b)(x, y) = \min_{u,v} (f(x+u), y+v) - b(u, v) \quad (2)$$

The dilation operation, $(f \oplus b)$, can expand the gray value of the image, and the erosion operation, $(f \ominus b)$, can reduce the gray value of the image because of the maximum and minimum operation. Based on dilation and erosion, the opening and closing of $f(x, y)$ by b , denoted by $f \circ b$ and $f \bullet b$, are defined by

$$(f \circ b)(x, y) = (f \ominus b) \oplus b \quad (3)$$

$$(f \bullet b)(x, y) = (f \oplus b) \ominus b. \quad (4)$$

The opening operation, $f \circ b$, can smooth the outline of an image, break the narrow connections between images, and eliminate tiny burrs. The closing operation, $f \bullet b$, can bridge the narrow gap between images and fill the holes. The opening and closing operations do not change the size of the target. Then, based on the opening operation and closing operations, the white top-hat transformation and black top-hat transformation of image f , denoted by wTH and bTH , respectively, are defined by

$$wTH(x, y) = f(x, y) - (f \circ b)(x, y) \quad (5)$$

$$bTH(x, y) = (f \bullet b)(x, y) - f(x, y) \quad (6)$$

White top-hat transformation (wTH) can effectively detect bright targets, whereas black top-hat transformation (bTH) can effectively detect dark targets.

C. Traditional Model for Infrared Small Target Detection

The infrared small target detection model can be uniformly written as follows:

$$I_D = I_T + I_B + I_N \quad (7)$$

where I_D , I_T , I_B , and I_N are the original infrared image, the target image, the background image, and the noise image, respectively. To achieve the purpose of infrared small target detection, on the one hand, we can suppress the background (I_B) and noise (I_N) of the input image (I_D). On the other hand, we can exploit the conversion operator to efficiently augment the target (I_T).

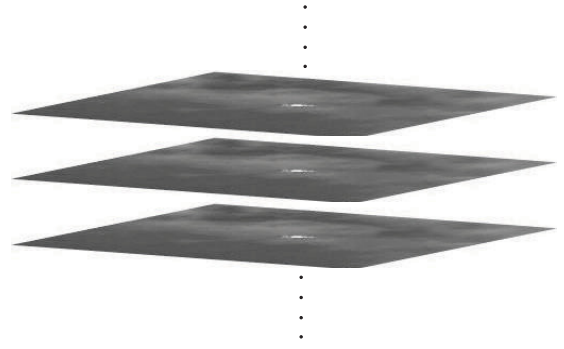


Fig. 1. Tensor of input image.

Gao *et al.* [2] have proposed that the small target detection task is a typical problem of intrinsically recovering a low-rank component and a sparse component from a data matrix. Ideally, this problem can be effectively addressed by solving the following formulation:

$$\min_{I_B, I_T} \text{rank}(I_B) + \alpha \|I_T\|_0 \quad \text{s.t.} \quad I_B + I_T = I_D \quad (8)$$

where $\text{rank}(I_B)$ denotes the rank of I_B and $\|*\|_0$ denotes the l_0 -norm of I_T which counts the number of nonzero entries.

III. METHOD FOR SMALL TARGET DETECTION

In this section, we introduce the properties of the proposed model in detail. We take a multiframe image and superimpose it into a tensor as the input image (\mathcal{I}_D). The detail of the tensor is described in Fig. 1. Then, we formulate a task for target detection to solve the Gaussian noise convex optimization minimization problem with the background low-rank and morphological operators as constraints. First, we introduce the characteristics of the target (\mathcal{I}_T), background (\mathcal{I}_B), and noise (\mathcal{I}_N), which provide a theoretical basis for the proposed tensor model. Furthermore, we present the whole method for target detection. Finally, we introduce the solution of each part separately, and the corresponding algorithm is explained in detail.

A. Ring Structural Element for Top-Hat Transformation

As revised in (3), the classic morphological theory usually uses two identical structuring elements in the procedure. However, it ignores the difference between the target area and the surrounding background area. In general, the target area is different from its surrounding background area. We can use the dissimilarity information between the target area and background area to model the differences, thus providing a small target with further highlights. Inspired by [36], we use a ring structuring element for top-hat transformation. The details of the structuring element are described in Fig. 2.

Let sBo and sBi represent two structuring elements with the same shape, and sBo is bigger than sBi . Let $s(Bo)$ and $s(Bi)$ represent the sizes of the structuring elements, sBo and sBi , respectively. We define a double-ring structuring element, $s1B$, and set $s1B = sBo - sBi$. $s(1B)$ is the radial distance from the center of $s1B$ to the outer edge of $s1B$. Let $s2B$

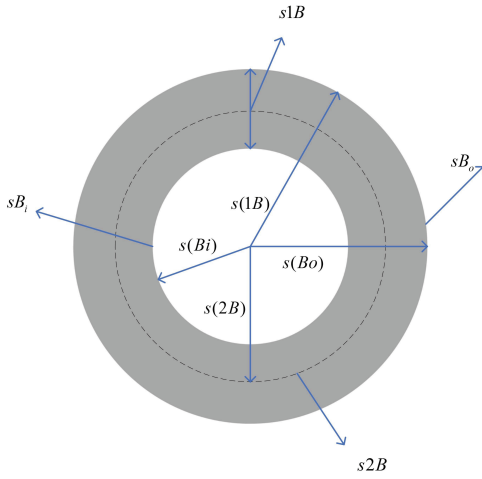


Fig. 2. Detail of structuring element.

represents the ring structuring element whose size is between sBo and sBi .

Then, the ring opening operation and closing operation, denoted by $f \triangleleft sB$ and $f \triangleright sB$, are defined by

$$(f \triangleleft sB)(x, y) = (f \oplus s1B) \ominus s2B \quad (9)$$

$$(f \triangleright sB)(x, y) = (f \ominus s1B) \oplus s2B. \quad (10)$$

Then, ring white top-hat transformation and black top-hat transformation of image, denoted by $nWTH$ and $nBTH$, are defined by

$$nWTH(x, y) = f(x, y) - (f \triangleleft sB)(x, y) \quad (11)$$

$$nBTH(x, y) = (f \triangleright sB)(x, y) - f(x, y) \quad (12)$$

where sB represents that the operation is related to sBo and sBi . Here, we use the ring morphology as a regular item to constrain the target.

The above-mentioned definitions indicate that the ring top-hat transformations are different from classical top-hat transformations.

For the formula (9), $f \oplus s1B$ first uses $s1B$ to replace the pixels of the target area with the pixels of target surrounding area. Then, $\ominus s2B$ operation uses $s2B$ calculate the difference between target surrounding area and target area. In this operation, regardless of the difference between the target area and the target surrounding area, the $s1B$ can introduce this difference information into the structural element.

In this article, we use the $W(\cdot)$ and $O_S(\cdot)$ to replace the $nWTH(\cdot)$ and $f \triangleright sB(\cdot)$. Therefore, we define the ring top-hat operator

$$W(\mathcal{I}_T) = \mathcal{I}_T - O_S(\mathcal{I}_T). \quad (13)$$

B. Low-Rank Tensor Model in Infrared Background

It is notable that a consistent local background prior is exploited, assuming that the background transitions slowly and the nearby pixels are highly correlated. We leverage

the low-rank property in the reconstruction stage. The initial assumption can be described as

$$\text{rank}(I_B) < k \quad (14)$$

where the constant k is determined by the background and k constrains the complexity of the background image. The value k of a complex background is larger than that of a uniform background.

However, rank minimization is an NP-hard problem, and the nuclear norm defined as $\|I_B\|_* := \sum_k \sigma_k(I_B)$ is typically utilized in rank-minimization problems. In addition, $\sigma_k(I_B)$ denotes the k th singular value of I_B since it is the close convex approximant to the rank (I_B) [25]. However, it has been indicated in [27] that NNM causes too much shrinking because of the low-rank components of the data. The Schatten p -norm can guarantee a more accurate recovery of the low-rank components and requires weaker isometric equivalence properties compared with the traditional trace norm. To add prior knowledge to different singular values, [28] proposed a weighted nuclear norm, which can be defined as

$$\|I_B\|_{w,p*} = \left(\sum_k w_k \sigma_k^p(I_B) \right)^{1/p} \quad (15)$$

where $w_k = 1/(\sigma_k + \varepsilon)$, and ε is a small positive scalar.

Since the matrix image is the mode-3 unfolding matrix of a tensor, the matrix image model can be considered as a special case of the tensor model. Since detecting an infrared small target in a single frame image only considers the low-rank structure in one unfolding, lacking the main structural information, it is not sufficient to address a complex scene. Therefore, it motivates us to think about whether we can use the other two unfolding modes. In fact, in a tensor composed of consecutive multiple images, each dimension can be regarded as a low-rank matrix by tensor decomposition. Their unfolding matrices are low rank, which is defined as

$$\text{rank}(\mathcal{I}_{\mathcal{B}(i)}) < k_i \quad (16)$$

where $\mathcal{I}_{\mathcal{B}(i)}$ is the mode i expansion matrix for $\mathcal{I}_{\mathcal{B}}$, and k_i are constants determined by the unfold matrices of the tensor ($\mathcal{I}_{\mathcal{B}}$).

Applying(16) to the tensor model can be written as

$$\sum_{j=1}^n \|\mathcal{I}_{\mathcal{B}(j)}\|_{w,p*} = \sum_{j=1}^n \left(\sum_k w_k \sigma_k^p(\mathcal{I}_{\mathcal{B}(j)}) \right)^{1/p} \quad (17)$$

where n denotes an n -order tensor.

C. Noise Estimate

In this article, we assume that the noise(I_N) is random and $\|I_N\|_F \leq \varepsilon$, where ε is a small constant. Then, we can obtain the following factor using (7)

$$\|I_D - I_T - I_B\|_F \leq \varepsilon \quad (18)$$

where $\|\cdot\|_F$ is the Frobenius norm (i.e., $\|I_N\|_F = (\sum_{ij} N_{ij}^2)^{1/2}$).

Applying (18) to the tensor model can be written as

$$\|\mathcal{I}_D - \mathcal{I}_T - \mathcal{I}_B\|_F \leq \varepsilon \quad (19)$$

D. Proposed Model for Small Target Detection

In this section, we present our proposed TCTHR model for infrared target detection.

1) Under the No Noise Assumption

First, we assume that the infrared sequence image has no noise. Therefore, (7) can be changed into

$$\mathcal{I}_D = \mathcal{I}_T + \mathcal{I}_B. \quad (20)$$

Then, the model can be considered as a minimization problem

$$\min_{\mathcal{I}_T, \mathcal{I}_B} \|\mathcal{I}_D - \mathcal{I}_B - \mathcal{I}_T\|_F^2. \quad (21)$$

Combined with (13) and (17), the model can be written as

$$\begin{aligned} \min_{\mathcal{I}_B, \mathcal{I}_T} \alpha \sum_{i=1}^3 u_i \|\mathcal{I}_{B(i)}\|_{w, s_p}^p + \beta W(\mathcal{I}_T) \\ \text{s.t. } \mathcal{I}_D = \mathcal{I}_T + \mathcal{I}_B. \end{aligned} \quad (22)$$

where α , β , and p are constants and u_i is the weight of the i th dimension.

2) Under the Random Noise Assumption

Now, we consider that the infrared sequence image involves random noise. Then, model (22) can be written as

$$\begin{aligned} \min_{\mathcal{I}_B, \mathcal{I}_T} \alpha \sum_{i=1}^3 u_i \|\mathcal{I}_{B(i)}\|_{w, s_p}^p + \beta W(\mathcal{I}_T) \\ \text{s.t. } \|\mathcal{I}_D - \mathcal{I}_T - \mathcal{I}_B\|_F \leq \varepsilon. \end{aligned} \quad (23)$$

To relax the inequality of the constraint of model (23), it can be converted into

$$\begin{aligned} \min_{N, B, T} \frac{1}{2} \|\mathcal{I}_N\|_F^2 + \alpha \sum_{i=1}^3 u_i \|\mathcal{I}_{B(i)}\|_{w, s_p}^p + \beta W(\mathcal{I}_T) \\ \text{s.t. } \mathcal{I}_D = \mathcal{I}_N + \mathcal{I}_B + \mathcal{I}_T. \end{aligned} \quad (24)$$

Considering the variability of each dimension of tensors, we introduce a variable \mathcal{Y}_i and make $\mathcal{I}_B = \mathcal{Y}_i, i = 1, 2, 3$. Then, the model can be written as

$$\begin{aligned} \min_{\mathcal{I}_N, \mathcal{I}_B, \mathcal{I}_T} \frac{1}{2} \|\mathcal{I}_N\|_F^2 + \alpha \sum_{i=1}^3 u_i \|(\mathcal{Y}_i)_{(i)}\|_{w, s_p}^p + \beta W(\mathcal{I}_T) \\ \text{s.t. } \mathcal{I}_D = \mathcal{I}_N + \mathcal{I}_B + \mathcal{I}_T, \mathcal{I}_B = \mathcal{Y}_i, \quad i = 1, 2, 3. \end{aligned} \quad (25)$$

We use the ADMM [39] to solve the model (25). The detailed algorithm is shown in Algorithm 1. Then, model (25) can be rewritten as

$$\begin{aligned} L(\mathcal{I}_N, \mathcal{I}_B, \mathcal{I}_T, \mathcal{I}_Z, \mathcal{Y}_i) \\ = \frac{1}{2} \|\mathcal{I}_N\|_F^2 + \alpha \sum_{i=1}^3 u_i \|(\mathcal{Y}_i)_{(i)}\|_{w, s_p}^p \\ + \beta W(\mathcal{I}_T) - \langle \mathcal{I}_Z, \mathcal{I}_N + \mathcal{I}_B + \mathcal{I}_T - \mathcal{I}_D \rangle \\ - \sum_{i=1}^3 \langle \mathcal{S}_i, \mathcal{I}_B - \mathcal{Y}_i \rangle + \frac{a}{2} \|\mathcal{I}_N + \mathcal{I}_B + \mathcal{I}_T - \mathcal{I}_D\|_F^2 \\ + \sum_{i=1}^3 \frac{\rho_i}{2} \|\mathcal{I}_B - \mathcal{Y}_i\|_F^2 \end{aligned} \quad (26)$$

where \mathcal{I}_Z and \mathcal{S}_i are Laplace factors, and a and ρ_i are penalty factors.

E. Solution of Our Proposed Model

In this section, we describe the solution process for each parameter of the model in detail.

1) Solution of Noise (\mathcal{I}_N)

The solution of Step 2.1 in Algorithm 1 is described below

$$\begin{aligned} \min_{\mathcal{I}_N} \frac{1}{2} \|\mathcal{I}_N\|_F^2 + \frac{a}{2} \|\mathcal{I}_N + \mathcal{I}_B + \mathcal{I}_T - \mathcal{I}_D\|_F^2 \\ - \langle \mathcal{I}_Z, \mathcal{I}_N + \mathcal{I}_B + \mathcal{I}_T - \mathcal{I}_D \rangle. \end{aligned} \quad (27)$$

Then, model (27) can be rewritten as

$$\min_{\mathcal{I}_N} \frac{1}{2} \|\mathcal{I}_N\|_F^2 + \frac{a}{2} \|\mathcal{I}_N + \mathcal{I}_B + \mathcal{I}_T - \mathcal{I}_D - \frac{\mathcal{I}_Z}{a}\|_F^2. \quad (28)$$

The solution can be given as

$$\mathcal{I}_N = \frac{1}{a+1} (\mathcal{I}_Z - a(\mathcal{I}_B + \mathcal{I}_T - \mathcal{I}_D)). \quad (29)$$

2) Solution of Target (\mathcal{I}_T)

The solution of Step 2.2 in Algorithm 1 is described below

$$\min_{\mathcal{I}_T} \beta W(\mathcal{I}_T) + \frac{a}{2} \left\| \mathcal{I}_N + \mathcal{I}_B + \mathcal{I}_T - \mathcal{I}_D - \frac{\mathcal{I}_Z}{a} \right\|_F^2. \quad (30)$$

Inspired by [40], the optimal solution of model (30) is presented in the model, and the corresponding subgradient can be obtained instead of the gradient because of its concave property

$$\beta \left(\frac{\delta}{\delta(\mathcal{I}_T)} W(\mathcal{I}_T) \right) + a \left(\mathcal{I}_N + \mathcal{I}_B + \mathcal{I}_T - \mathcal{I}_D - \frac{\mathcal{I}_Z}{a} \right) = 0. \quad (31)$$

Then, the corresponding iteration can be written as

$$\begin{aligned} \mathcal{I}_T^{(n+1)} = \mathcal{I}_D^{(n+1)} + \frac{\mathcal{I}_Z}{a} - \mathcal{I}_N^{(n+1)} \\ - \mathcal{I}_B^{(n+1)} - \frac{\beta}{a} \left(\frac{\delta}{\delta(\mathcal{I}_T)} W(\mathcal{I}_T) \right)_{\mathcal{I}_T^{(n)}}. \end{aligned} \quad (32)$$

In the solution to (32), we derive the subgradients of the dilated and eroded image with respect to its pixel values. Let us denote the subgradient of a dilated image $D_{s1}(\mathcal{I}_T)$ as $\delta D_{s1}/\delta \mathcal{I}_T$ and that of an eroded image $E_{s2}(\mathcal{I}_T)$ as $\delta E_{s2}/\delta \mathcal{I}_T$. We can then write the subgradients of the dilated image and eroded image of j th element of the i th column as

$$\frac{\delta D_{s1, j}}{\delta t_i} = \begin{cases} 1, & \text{if } t_i = \max_{g \in (s1B)(j)} \{t_g\} \\ 0, & \text{if } t_i < \max_{g \in (s1B)(j)} \{t_g\} \end{cases} \quad (33)$$

$$\frac{\delta E_{s2, j}}{\delta t_i} = \begin{cases} 1, & \text{if } t_i = \min_{g \in (s2B)(j)} \{t_g\} \\ 0, & \text{if } t_i > \min_{g \in (s2B)(j)} \{t_g\} \end{cases} \quad (34)$$

where $s1B$ is a double-ring structuring element of size $s1$, $s2B$ is a concentric structuring element of size $s2$, $s1B(j)$ and $s2B(j)$ are sets of pixels covered under $s1B$ and $s2B$ translated to the j th pixel t_j respectively, and $\{t_g\}$ is a set of g .

Algorithm 1 ADMM for Solving Model (25)

-
- 1: Step 0: **Input:** $\mathcal{I}_{\mathcal{D}}, \mathcal{I}_{\mathcal{Z}} = 1$,
2: Step 1: **Initialize:** $\mathcal{I}_{\mathcal{B}} = \mathcal{I}_{\mathcal{D}}, \mathcal{Y}_i = \mathcal{I}_{\mathcal{B}}, \mathcal{I}_{\mathcal{N}} = 0, \mathcal{I}_{\mathcal{T}} = 0$
3: Step 2: **While** not converge **do**
 Step 2.1: $\min_{\mathcal{I}_{\mathcal{N}}} \frac{1}{2} \|\mathcal{I}_{\mathcal{N}}\|_F^2 + \frac{a}{2} \|\mathcal{I}_{\mathcal{N}} + \mathcal{I}_{\mathcal{B}} + \mathcal{I}_{\mathcal{T}} - \mathcal{I}_{\mathcal{D}}\|_F^2 - \langle \mathcal{I}_{\mathcal{Z}}, \mathcal{I}_{\mathcal{N}} + \mathcal{I}_{\mathcal{B}} + \mathcal{I}_{\mathcal{T}} - \mathcal{I}_{\mathcal{D}} \rangle$
 Step 2.2: $\min_{\mathcal{I}_{\mathcal{T}}} \beta W(\mathcal{I}_{\mathcal{T}}) + \frac{a}{2} \|\mathcal{I}_{\mathcal{N}} + \mathcal{I}_{\mathcal{B}} + \mathcal{I}_{\mathcal{T}} - \mathcal{I}_{\mathcal{D}} - \frac{\mathcal{I}_{\mathcal{Z}}}{a}\|_F^2$
 Step 2.3: $\min_{\mathcal{I}_{\mathcal{B}}} \left\{ \frac{a}{2} \|\mathcal{I}_{\mathcal{N}} + \mathcal{I}_{\mathcal{B}} + \mathcal{I}_{\mathcal{T}} - \mathcal{I}_{\mathcal{D}} - \frac{\mathcal{I}_{\mathcal{Z}}}{a}\|_F^2 + \sum_{i=1}^3 \frac{\rho_i}{2} \|\mathcal{I}_{\mathcal{B}} - \mathcal{Y}_i - \frac{\mathcal{S}_i}{\rho_i}\|_F^2 \right\}$
 Step 2.4: $\min_{\mathcal{Y}_i} a u_i \|(\mathcal{Y}_i)_{(i)}\|_{w,sp}^p + \frac{\rho_i}{2} \|\mathcal{Y}_i - \left(\mathcal{I}_{\mathcal{B}} - \frac{\mathcal{S}_i}{\rho_i} \right)\|_F^2$
4: Step 3: **Output**
-

We can write the subgradients of the ring top-hat operator as

$$\begin{aligned} \frac{\delta}{\delta(\mathcal{I}_{\mathcal{T}})} W(\mathcal{I}_{\mathcal{T}}) &= \mathcal{I} - \frac{\delta}{\delta(\mathcal{I}_{\mathcal{T}})} O_S(\mathcal{I}_{\mathcal{T}}) \\ &= \mathcal{I} - \frac{\delta}{\delta(\mathcal{I}_{\mathcal{T}})} E_{S_2}(D_{S_1}(\mathcal{I}_{\mathcal{T}})) \\ &= \mathcal{I} - \frac{\delta}{\delta D_{S_1}(\mathcal{I}_{\mathcal{T}})} E_{S_2}(D_{S_1}(\mathcal{I}_{\mathcal{T}})) \frac{\delta}{\delta(\mathcal{I}_{\mathcal{T}})} D_{S_1}(\mathcal{I}_{\mathcal{T}}) \end{aligned} \quad (35)$$

By combining (33) and (34) with the dilation operation $D_{s_1}(\mathbf{X}) = [d_{s_1,1}, d_{s_1,2}, \dots, d_{s_1,mn}]$ of the s th scale, the calculation of $[\delta/\delta D_{S_1}(\mathcal{I}_{\mathcal{T}})] E_{S_2}[D_{S_1}(\mathcal{I}_{\mathcal{T}})]$ is presented as follows:

$$q_i^{E_{S_2,j}} = \frac{\delta E_{S_2,j}}{\delta d_{s_1,i}} = \begin{cases} 1, & \text{if } d_{s_1,i} = \min_{r \in (s_2B)(j)} \{d_{s_1,r}\} \\ 0, & \text{if } d_{s_1,i} > \min_{r \in (s_2B)(j)} \{d_{s_1,r}\} \end{cases}. \quad (36)$$

Substituting (33)–(36), we can compute the subgradient of $[\delta(W(\mathcal{I}_{\mathcal{T}}))/\delta(\mathcal{I}_{\mathcal{T}})]$ which is required to compute the model (32).

3) Solution of Background ($\mathcal{I}_{\mathcal{B}}$)

The solution of Step 2.3 in Algorithm 1 is described below

$$\min_{\mathcal{I}_{\mathcal{B}}} \left\{ \frac{a}{2} \left\| \mathcal{I}_{\mathcal{N}} + \mathcal{I}_{\mathcal{B}} + \mathcal{I}_{\mathcal{T}} - \mathcal{I}_{\mathcal{D}} - \frac{\mathcal{I}_{\mathcal{Z}}}{a} \right\|_F^2 + \sum_{i=1}^3 \frac{\rho_i}{2} \left\| \mathcal{I}_{\mathcal{B}} - \mathcal{Y}_i - \frac{\mathcal{S}_i}{\rho_i} \right\|_F^2 \right\}. \quad (37)$$

The minimizer

$$\mathcal{I}_{\mathcal{B}} = \frac{a(\mathcal{I}_{\mathcal{D}} - \mathcal{I}_{\mathcal{N}} - \mathcal{I}_{\mathcal{T}}) + \mathcal{I}_{\mathcal{Z}} + \sum_{i=1}^3 (\rho_i \mathcal{Y}_i + \mathcal{S}_i)}{a + \rho_1 + \rho_2 + \rho_3}. \quad (38)$$

4) Solution of \mathcal{Y}_i

The solution of Step 2.4 in Algorithm 1 is described below

$$\min_{\mathcal{Y}_i} a u_i \|(\mathcal{Y}_i)_{(i)}\|_{w,sp}^p + \frac{\rho_i}{2} \left\| \mathcal{Y}_i - \left(\mathcal{I}_{\mathcal{B}} - \frac{\mathcal{S}_i}{\rho_i} \right) \right\|_F^2 \quad (39)$$

where $i = 1, 2, 3$. Then, model (39) can be rewritten as

$$\min_{\mathcal{Y}_i} \frac{2a u_i}{\rho_i} \|(\mathcal{Y}_i)_{(i)}\|_{w,sp}^p + \left\| \mathcal{Y}_i - \left(\mathcal{I}_{\mathcal{B}} - \frac{\mathcal{S}_i}{\rho_i} \right) \right\|_F^2 \quad (40)$$

Algorithm 2 Solution Model (40) via Generalized Soft Thresholding

-
- 1: **Input:** $X, \{w_j\}_{j=1}^r$ in non-descending order, l , and p .
2: **Output:** Y
3: $X = U \Sigma V^T, \Sigma = \text{diag}(\delta_1, \dots, \delta_r)$;
4: **for** $j = 1$ to r
5: $\tau(w_j) = (2w_j(1-p))^{\frac{1}{2-p}} + wp(2w_j(1-p))^{\frac{p-1}{2-p}}$
6: **if** $|\delta_j| \leq \tau(w_j)$
7: $\sigma_j = 0$;
8: **else** $|\delta_j| \leq \tau(w_j)$
9: $\sigma_0 = |\delta_j|$;
10: **for** $i = 0, 1, \dots, l$
11: $\sigma_{i+1} = |\delta_j| - w_j p(\sigma_i)^{p-1}$;
12: $i = i + 1$;
13: **end**
14: $\sigma_j = \text{sgn}(\delta_j) \sigma_j$;
15: **end**
16: **end**
17: $\Delta = \text{diag}(\sigma_1, \dots, \sigma_r)$;
18: $Y = U \Delta V^T$.
-

where $2a u_i / \rho_i$ is a tradeoff parameter to balance the data fidelity and regularization. Here, inspired by [28], we solved model (40) using Algorithm 2. Let $\mathcal{G} = \mathcal{I}_{\mathcal{B}} - \mathcal{S}_i / \rho_i$, we compute all of the \mathcal{G} mode expansion matrices and finally calculate the average. First, $\mathcal{G}_i = U \Sigma V^T$ by SVD, where \mathcal{G}_i indicates the mode i of \mathcal{G} , and $\Sigma = \text{diag}(\delta_1, \dots, \delta_r)$, where $r = \min(m, n)$. Suppose all the singular values are arranged in nonincreasing order, then the solution of model (40) is be $Y_i = U \Delta V^T$ with $\Delta = \text{diag}(\sigma_1, \dots, \sigma_r)$, where σ is given.

IV. EXPERIMENTAL RESULTS AND DISCUSSION

In this section, we make use of a series of structural experiments to illustrate the performance of the proposed method. First, we introduce the evaluation metrics and the baseline methods for comparison in this article. After that, we discuss the effects of the parameters of the proposed method and the information of real image sequences by performing simulation experiments. Finally, we perform experiments on real image sequences to evaluate the performance of the proposed method.

A. Evaluation Metrics and Baseline Methods

1) *Evaluation Metrics*: The probability of detection and false alarm rate are the most important metrics to quantify the performance of small target detection methods. The probability of detection represents the probability that the true target is determined as the target, and the false alarm rate represents the probability that a false target is determined as the target, which can be defined as follows:

$$Pd = \frac{\text{number of true infrared targets}}{\text{number of actual infrared targets}} \quad (41)$$

$$Fa = \frac{\text{number of false infrared targets}}{\text{number of all test infrared images}}. \quad (42)$$

In this article, it is noticeable that the target position is detected if the detection result satisfies two requirements at the same time: 1) the real target and the detection result have overlapping pixels and 2) the distance between the real target center and the detection result center pixel is at a threshold (three pixels) inside.

The SCR gain (SCRG) and the background suppression factor (BSF) are also commonly used indicators to detect the performance of small target detection methods [6]. Larger SCRG and BSF values indicate better small target enhancement and background suppression.

2) *Baseline Methods*: To prove the superiority and robustness of the proposed method, we use different baseline methods for comparison.

- 1) *Weighted Local Difference Measure [17]*: WLDM is a method of using multiscale local difference priors around the target.
- 2) *Infrared Patch Image Model [2]*: IPM exploits the low rank of nonlocal backgrounds and the sparseness of targets to translate target detection problems into low-rank and sparse recovery problems.
- 3) *Directional Saliency-Based Method [20]*: Using the difference in optical point spread between the infrared small target and the background, DSBM formulates the target detection problem as significant area detection.
- 4) *Spatio-Temporal Saliency Approach [19]*: STSA uses the temporal saliency and spatial saliency information between different image frames and proposes a local adaptive contrast operation to extract the spatiotemporal saliency map of tensor data.
- 5) *New Top-Hat Transform [36]*: NTHT defines two different but related structural elements to enhance the classic top hat transformation and consider the difference information between the target and the surrounding area.
- 6) *Reweighted Infrared Patch Tensor [6]*: RIPT proposes a novel reweighted infrared patch-tensor model based on nonlocal self-correlation in patch space and local structure prior of the target.

B. Setting of Parameters and the Data Sets

In this section, we discuss the effects of the parameters in our proposed method, including the values of p , the sharp of the structuring element. After that, we perform seven real image experiments to evaluate the effects of different values of

TABLE I
COMPARISON THROUGH DIFFERENT TOP-HAT REGULARIZATION

Sequence	<i>Classical</i> <i>top-hat</i>		<i>Ring</i> <i>top-hat</i>	
	SCRG	BSF	SCRG	BSF
seq1	12.482	12.102	19.963	20.525
seq2	8.153	7.9815	28.886	29.317
seq3	3.181	3.160	5.026	5.099
seq4	6.261	6.158	13.649	14.559
seq5	9.357	9.071	12.463	13.025
seq6	5.428	5.295	10.357	10.424
seq7	3.429	3.332	3.855	5.510

p on the traditional morphological constraints and ring morphological constraints. Finally, we describe the information of the real image sequences and compare the 3D maps of the different methods in the different image sequences.

1) *Parameter Settings*: In the following experiments, we compared the results in modeling with traditional top-hat regularization and ring top-hat regularization. To verify the superiority of ring top-hat regularization, we randomly select several experimental results and calculate the average SCRG and BSF, which are listed in Table I. We can clearly see the improvement of the indicator, which also proves that the ring top-hat regularization can utilize the information of the target and surrounding pixels and improve the performance of the detection.

In this article, we choose a larger size of $s2B$ and a smaller size of $s1B$ when fixing $sB0$. We set $s2B = sB0$, $sB0$, and sBi as closely as possible in this article. Regarding the setting of the parameter $sB0$, we need to consider the shape of the target. In general, the more similar $sB0$ is to the target, the better the effect, including the shape of the structuring element and the size of its pixels.

In this recovery of background, the value of p in the weighted Schatten p -norm is especially important. Through experiments, we fixed the value of p to 0.1. The detailed is shown as Section IV-D.

For our proposed model, we set $2\alpha W_i/\rho_i$, which is an important parameter for optimization, to $1/\sqrt{m}$, according to the original work, where m is the number of rows of the matrix obtained when the tensor is expanded in mode i . For our model, we set $w_j = 1/(\delta_j(X) + \varepsilon)$, and $\varepsilon = 10^{-16}$, where ε prevents the denominator from becoming zero.

2) *Data Sets*: To facilitate visualizing the test data, we have shown a single-frame image of each of the different test sequences and the corresponding 3D map in Fig. 3.

Taking the diversity of the goals and the complexity of the background into account, we used multiple real sequence images to test our proposed method. In sequence 1, the target is a slow-moving airplane, and the background is covered by a large number of clouds. In sequence 2, the target is a long-distance, regular-shaped ship, and there is a blurred sea-sky background. In sequence 3, the target is a moving, irregularly shaped aircraft, and there is a heavy sky cluttered background. In sequence 4, the target is a moving, irregularly shaped ship, and there is a blurred sea-sky background. In sequence 5, the target is a moving, regular-shaped helicopter, and there is a heavy sky cluttered background. In sequence 6, the target is a short-distance, regular-shaped ship and there is a blurred

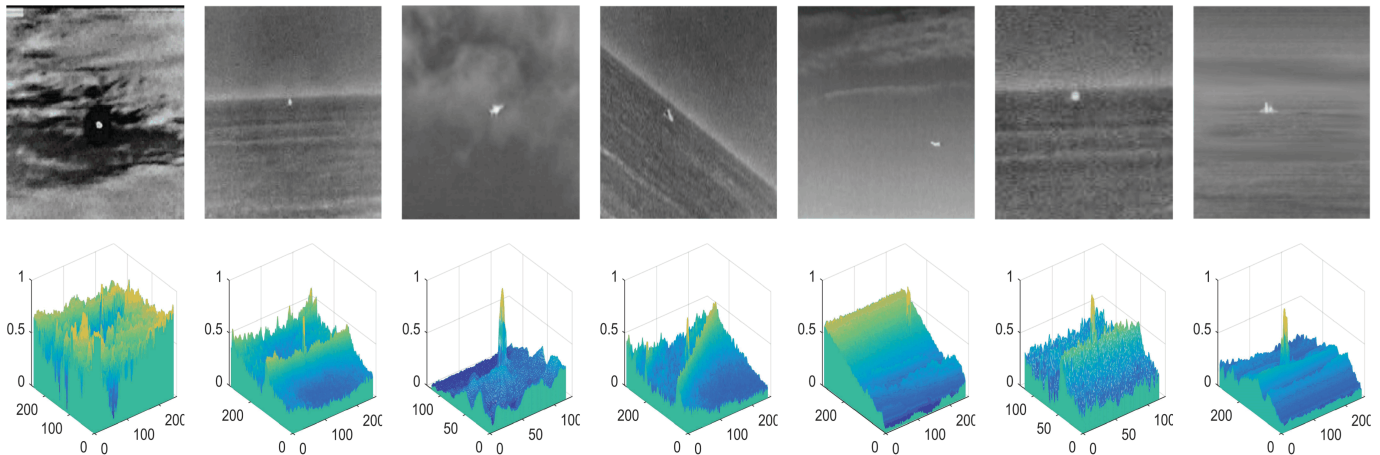


Fig. 3. Real infrared image. The first row denotes the seven real image sequences, and the second row denotes the corresponding 3D gray distributions.

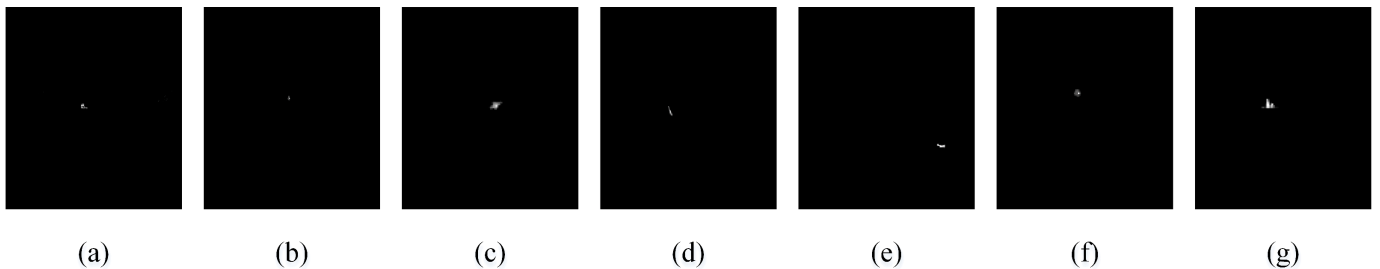


Fig. 4. (a1)–(a7) Denote the detected results of seven real images by using our method.

TABLE II
DETAILS OF REAL IMAGE SEQUENCES

	Frames	Image size	Target size	Target type	Target details	Background details
sequence1	63	220 * 220	5 * 5 ~ 5 * 7	An airplane	A long imaging distance Keeping motionless	Heavy sky clutter background Heavy noise
sequence2	101	320 * 196	4 * 4 ~ 5 * 5	A small ship	A small size A short imaging distance	Blurred sea-sky background Almost keeping the same
sequence3	81	128 * 128	5 * 6 ~ 5 * 8	An airplane	Keeping motion A bright target	Heavy sky clutter background Changing background
sequence4	107	320 * 196	4 * 6 ~ 5 * 6	A small ship	A short imaging distance Keeping motion	Blurred sea-sky background Changing background
sequence5	40	256 * 176	3 * 8 ~ 3 * 9	A helicopter	Keeping motion An unchanging size	Heavy sky clutter background Heavy noise
sequence6	100	128 * 128	4 * 4 ~ 5 * 5	A small ship	A short imaging distance Keeping motionless	Almost keeping the same Blurred sea-sky background
sequence7	63	124 * 124	6 * 6 ~ 11 * 12	A ship	A bright target A changing size	Heavy sea clutter background Almost keeping the same

sea-sky background. In sequence 7, the target is a fast-moving ship with an irregular shape, and there is a heavy sea clutter background. The details of each image include a heavy sea cluttered background. The details of each image sequence are described in Table II. Furthermore, we present the detected results of seven original images in Fig. 4.

To evaluate our proposed method, we compare the 3D maps of the different methods. The results of each image sequence are shown in Fig. 5. From the 3D map of the target obtained using our proposed method, we can see that the target area is very prominent and that the proposed method suppressed the background well. Fig. 5(e1)–(e7), show that the performance

of the NTHT [36] method is not ideal. The target area is much cluttered, and it is difficult to distinguish the target location. It can be seen from Fig. 5(f1)–(f7) that the target area has been enhanced, but its clutter is too much, and background suppression is not good. Obviously, our proposed method has most outstanding performance for all the seven real image sequences.

C. Tests on Real Images

In this section, we perform numerous experiments to demonstrate the superiority of our method. First, we com-

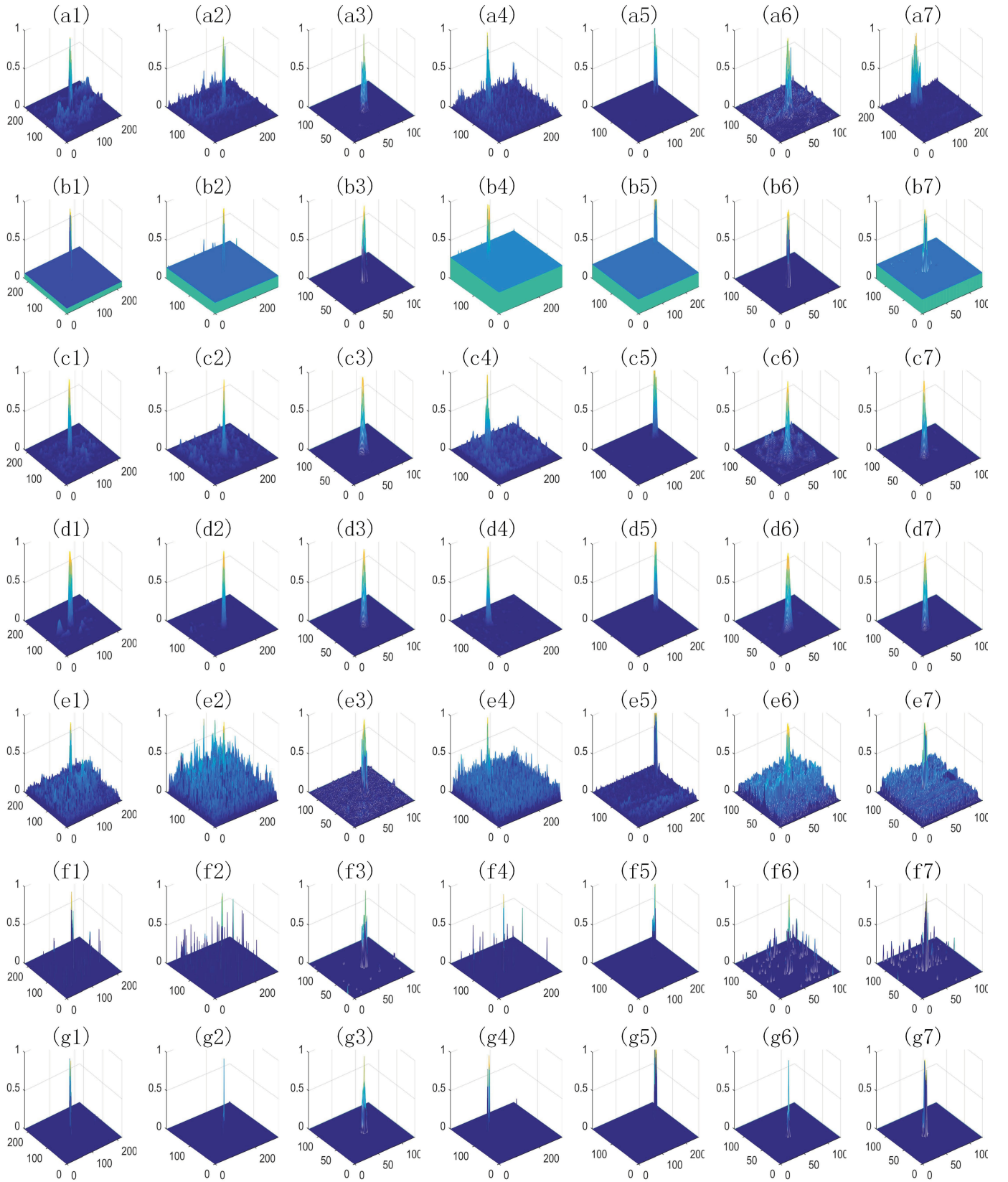


Fig. 5. Enhanced results obtained through different baseline methods. (a1)–(a7), (b1)–(b7), (c1)–(c7), (d1)–(d7), (e1)–(e7), (f1)–(f7), and (g1)–(g7) Enhanced results obtained by using the WLDB, IPM, DSBM, STSA, NHTT, RIPT, and our method, respectively.

pare the BSF and SCRGR values of different real image sequences with different methods. In addition, we compared the Pd and Fa of each sequence and plotted the receiver

operating characteristic curve (ROC) plot. Finally, we compared the area under curve (AUC) values of the different sequences.

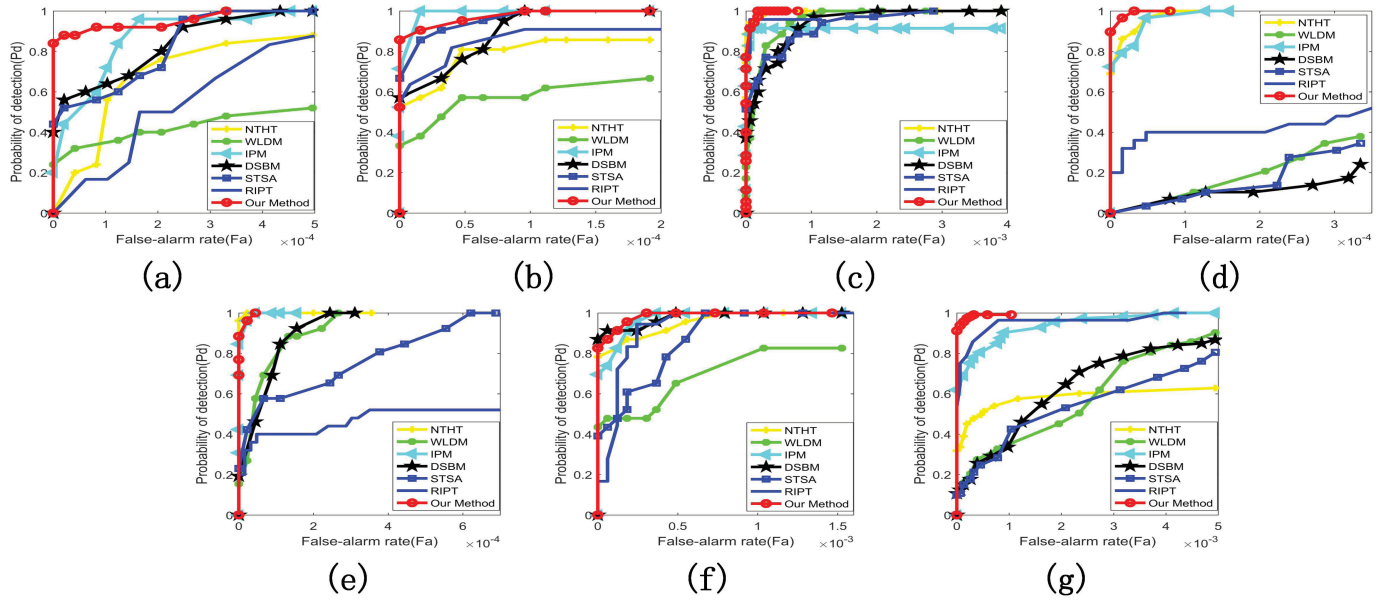


Fig. 6. Characteristic (ROC) curves of six methods for the seven real image sequences. (a) Real image sequence 1. (b) Real image sequence 2. (c) Real image sequence 3. (d) Real image sequence 4. (e) Real image sequence 5. (f) Real image sequence 6. (g) Real image sequence 7.

TABLE III
AVERAGE VALUES OF SCRG AND BSF OBTAINED THROUGH DIFFERENT METHODS

	WLDM		IPM		DSBM		STSA		NTHT		RIPT		Our Method	
	SCRG	BSF	SCRG	BSF	SCRG	BSF	SCRG	BSF	SCRG	BSF	SCRG	BSF	SCRG	BSF
seq1	7.448	6.095	12.649	11.399	12.704	6.281	5.331	5.568	4.358	5.625	19.248	15.629	19.958	20.449
seq2	3.457	10.534	6.773	5.673	3.443	2.596	5.484	5.423	1.219	3.088	6.781	6.689	28.897	29.349
seq3	2.231	5.348	2.194	2.154	2.180	1.539	2.993	2.429	1.635	3.766	3.426	3.281	5.025	5.100
seq4	10.459	14.181	6.163	4.809	4.877	2.217	10.444	5.039	1.589	3.615	10.590	9.524	13.666	14.829
seq5	7.694	23.395	7.939	6.872	8.536	4.510	16.248	7.288	4.686	11.254	12.897	12.471	12.445	12.967
seq6	2.197	6.665	2.884	2.415	2.071	1.986	2.686	2.683	0.850	2.092	4.539	3.550	10.352	10.420
seq7	1.639	6.637	2.626	2.333	2.527	1.287	2.433	2.034	1.065	2.880	3.716	3.206	3.854	5.512

TABLE IV
AVERAGE VALUES OF Pd AND Fa OBTAINED THROUGH DIFFERENT METHODS

	WLDM		IPM		DSBM		STSA		NTHT		RIPT		Our Method	
	P_d	F_a	P_d	F_a	P_d	F_a	P_d	F_a	P_d	F_a	P_d	F_a	P_d	F_a
seq1	0.490	0.412	0.852	0.126	0.833	0.158	0.728	0.252	0.827	0.316	0.857	0.222	0.807	0.126
seq2	0.817	0.188	0.980	0.069	0.881	0.010	0.968	0.051	0.832	0.010	0.909	0.059	0.943	0.010
seq3	0.907	0.135	0.784	0.012	0.971	0.197	0.872	0.111	0.865	0.012	0.875	0.012	0.911	0.012
seq4	0.519	0.542	0.952	0.037	0.514	0.252	0.559	0.140	0.770	0.065	0.520	0.495	0.961	0.009
seq5	0.898	0.250	0.946	0.050	0.844	0.175	0.826	0.275	0.976	0.050	0.905	0.075	0.984	0.025
seq6	0.619	0.100	0.937	0.020	0.933	0.030	0.801	0.060	0.899	0.050	0.944	0.060	0.974	0.010
seq7	0.603	0.365	0.878	0.111	0.718	0.285	0.643	0.301	0.760	0.380	0.857	0.079	0.961	0.031

TABLE V
VALUES OF AUC OBTAINED THROUGH DIFFERENT METHODS

	WLDM	IPM	DSBM	STSA	NTHT	RIPT	Our Method
seq1	0.4217	0.8600	0.8250	0.8142	0.6717	0.7982	0.9508
seq2	0.5694	0.9881	0.8829	0.9544	0.7857	0.8941	0.9722
seq3	0.9515	0.9123	0.9355	0.9275	0.9955	0.9496	0.9958
seq4	0.1765	0.9704	0.1010	0.1494	0.9787	0.4755	0.9959
seq5	0.9082	0.9963	0.9094	0.7543	0.9994	0.9003	0.9969
seq6	0.6922	0.9704	0.9783	0.8600	0.9513	0.9843	0.9852
seq7	0.5716	0.9361	0.6238	0.5321	0.5815	0.9603	0.9926

For the successive several frame images randomly selected from the seven real infrared image sequences, the average values of the BSF and SCRG obtained using WLDB [17], IPM [2], DSBM [20], STSA [19], NTHT [36], RIPT [6],

and our method are listed in Table III. We find that the indicator values of the baseline methods are low, while our proposed method improved the indicator value of these images significantly. Table III shows that the indicator values of the NTHT [36] method are small, and the RIPT [6] method has a better performance than the other baseline methods for the seven real sequences. Overall, our proposed method has the best performance for all seven real image sequences. These experimental results show that our method can significantly highlight the goals and better suppress the background.

In addition, we computed the corresponding Pd and Fa for the earlier images. The details are listed in Table IV. We find that the results of the other baseline methods are poor, while the proposed method can improve the performance of these images significantly. Table IV shows that the performance of

TABLE VI
VALUES OF SCRG AND BSF OBTAINED THROUGH RING TOP-HAT REGULARIZATION BY USING DIFFERENT VALUE OF p

Sequence	$p = 0.1$		$p = 0.3$		$p = 0.5$		$p = 0.7$		$p = 0.9$	
	SCRG	BSF	SCRG	BSF	SCRG	BSF	SCRG	BSF	SCRG	BSF
seq1	19.985	20.449	20.156	20.732	20.104	20.706	20.188	20.725	20.195	20.613
seq2	28.897	29.349	28.873	29.315	28.848	29.296	28.798	29.263	28.744	29.198
seq3	5.025	5.100	5.021	5.090	5.015	5.080	5.009	5.070	5.001	5.059
seq4	13.666	14.829	13.579	14.433	13.558	14.556	13.546	14.569	13.520	14.703
seq5	12.445	12.967	12.395	12.965	12.452	12.971	12.492	13.084	12.455	12.977
seq6	10.352	10.420	10.329	10.393	10.279	10.341	10.250	10.315	10.219	10.291
seq7	3.854	5.512	3.848	5.499	3.835	5.4738	3.825	5.456	3.816	5.437

the NTHT [36] method in terms of Pd and Fa is not ideal and that the IPM [2] method has a better performance. When keeping Fa constant, we can see that the Pd value of our proposed method is higher than that of the baseline methods. Overall, our proposed method has an outstanding performance for all seven real image sequences. These experimental results show that our proposed method can significantly highlight the goals, better suppress the background and identify targets more accurately.

The characteristic ROC curve is a graphical plot of the detection probabilities versus the false alarm rates. We provide the ROC curves obtained by the baseline methods and the proposed method for the seven image sequences in Fig. 6. We see that our method has a better performance than the baseline methods, especially for real sequences 3, 4, and 7. The horizontal axis of the ROC curve is the Fa of the sequence. The vertical axis is the Pd of the sequence. In addition, we calculate the area under the curve AUC of each method. The area under the ROC curve is widely utilized to evaluate the classification performance of true or false targets. The values of the AUC are within the range of 0–1. A larger AUC value means a better target detection performance in the ROC curve evaluation system. The AUC values are shown in Table V. We can find that the AUC values of our proposed method are larger than those of the baseline methods, which means that our proposed method can better detect the target.

D. Parameter Analysis

In this article, the value of p in the weighted Schatten p -norm is especially important for the detection result. From the above-mentioned definition, we know that the Schatten p -norm degenerates to the nuclear norm when p is taken as 1. Therefore, to achieve a better target detection effect, we set different p -values and conducted comparative experiments when the values of p are taken as $p = 0.1, 0.3, 0.5, 0.7, \text{ and } 0.9$. We have listed the specific indicators in Table VI.

Here, we visually see the p -value corresponding to the highest value of the indicator for different sequence data. For sequence 1, the indicators reach a peak when the value of p is 0.3 and 0.9. For sequence 5, the indicators reach a peak when the value of p is 0.7. However, for sequences 2, 3, 4, 6, and 7, the indicators reach a peak when the value of p is 0.1. Therefore, after weighing all the experimental results in Table VI, we chose $p = 0.1$ in this article.

E. Complexity Analysis and Running Time

Here, we discuss the computational complexity of our model and real running time with detailed specification of the running environment. As shown in Algorithm 1, the algorithm complexity is mainly composed of two parts: the solution of target and generalized soft-thresholding computation (Algorithm 2). Here, we define that the image size is $M \times N$, and m, n are the rows and columns of the mode-3 unfolding.

For the solution of the target, the computational complexity is mainly determined by the ring top-hat regularization. The dilate operation is computed in $O(m \times n)$ time, and therefore, the ring open operation can be computed in $O(m^2 \times n^2)$. For the generalized soft thresholding, the computational complexity is mainly composed of two parts: the complexity of SVD (Algorithm 2, step 1) needs $O(m \times n)$; the complexity of others step needs $O(r \times l)$, where, r is the number of nonzero singular values, and l is the number of iterations in the generalized soft thresholding. The computational complexity of generalized soft thresholding is $O(m \times n + r \times l)$. Based on the earlier analysis, the computational complexity of our model is around $O(k(m^2 \times n^2 + m \times n + r \times l))$, where k is the iteration number of the algorithm. Taking sequence 4 as an example, the complexity is $O(km^2n^2)$, and we perform the test using MATLAB R2016a on a laptop with Intel Core i5-4210 CPU and 4-GB RAM, and the computational time is 10.30 s.

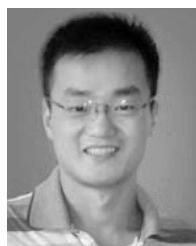
V. CONCLUSION

This article proposes a TCTHR model for the purpose of infrared small target detection based on low-rank tensor completion and ring top-hat regularization, which can be solved efficiently using ADMM. Combining the structural characteristics of low-rank tensors and the prior knowledge of the structure of morphological structuring elements, our model has achieved good infrared small target detection performance. Through the experiments, we can intuitively observe that the algorithm not only significantly increases the SCR and BSF values of the image but also achieves a high-accuracy level and low false alarm rate. We conducted many experiments on the background of small target images in different complex scenes, showing that our method is significantly better than the classic methods.

REFERENCES

- [1] M. Zeng, J. Li, and Z. Peng, "The design of top-hat morphological filter and application to infrared target detection," *Infr. Phys. Technol.*, vol. 48, no. 1, pp. 67–76, Apr. 2005.

- [2] C. Q. Gao, D. Meng, Y. Yang, Y. Wang, X. Zhou, and A. G. Hauptmann, "Infrared patch-image model for small target detection in a single image," *IEEE Trans. Image Process.*, vol. 22, no. 12, pp. 4996–5009, Dec. 2013.
- [3] Y. He, M. Li, J. Zhang, and Q. An, "Small infrared target detection based on low-rank and sparse representation," *Infr. Phys. Technol.*, vol. 68, pp. 98–109, Jan. 2015.
- [4] J. Liu, P. Musialski, P. Wonka, and J. Ye, "Tensor completion for estimating missing values in visual data," *IEEE Trans. Pattern Anal. Mach. Intell.*, vol. 35, no. 1, pp. 208–220, Jan. 2013.
- [5] H. N. Phien, H. D. Tuan, J. A. Bengua, and M. N. Do, "Efficient tensor completion: Low-rank tensor train," 2006, *arXiv:1601.01083*. [Online]. Available: <https://arxiv.org/abs/1601.01083>
- [6] Y. Dai and Y. Wu, "Reweighted infrared patch-tensor model with both nonlocal and local priors for single-frame small target detection," *IEEE J. Sel. Topics Appl. Earth Observ. Remote Sens.*, vol. 10, no. 8, pp. 3752–3767, Aug. 2017.
- [7] C. L. P. Chen, H. Li, Y. Wei, T. Xia, and Y. Y. Tang, "A local contrast method for small infrared target detection," *IEEE Trans. Geosci. Remote Sens.*, vol. 52, no. 1, pp. 574–581, Jan. 2014.
- [8] X. Wang, L. T. Yang, H. Li, M. Lin, J. Han, and B. O. Apduhan, "NQA: A nested anti-collision algorithm for RFID systems," *ACM Trans. Embedded Comput. Syst.*, vol. 18, no. 4, 2019, Art. no. 32.
- [9] M. Malanowski and K. Kulpa, "Detection of moving targets with continuous-wave noise radar: Theory and measurements," *IEEE Trans. Geosci. Remote Sens.*, vol. 50, no. 9, pp. 3502–3509, Sep. 2012.
- [10] S. Kim and J. Lee, "Scale invariant small target detection by optimizing signal-to-clutter ratio in heterogeneous background for infrared search and track," *Pattern Recognit.*, vol. 45, no. 1, pp. 393–406, Jan. 2012.
- [11] L. Deng, H. Zhu, C. Tao, and Y. Wei, "Infrared moving point target detection based on spatial-temporal local contrast filter," *Infr. Phys. Technol.*, vol. 76, pp. 168–173, May 2016.
- [12] G.-Y. Wang, Z.-X. Chen, and Q.-L. Li, "A review of infrared weak and small targets detection under complicated background," *Infr. Technol.*, vol. 28, pp. 287–292, May 2006.
- [13] H. Zhu, Y. Guan, L. Deng, Y. Li, and Y. Li, "Infrared moving point target detection based on an anisotropic spatial-temporal fourth-order diffusion filter," *Comput. Elect. Eng.*, vol. 68, pp. 550–556, May 2018.
- [14] J. Han, Y. Ma, J. Huang, X. Mei, and J. Ma, "An infrared small target detecting algorithm based on human visual system," *IEEE Geosci. Remote Sens. Lett.*, vol. 13, no. 3, pp. 452–456, Mar. 2016.
- [15] S. D. Deshpande, M. H. Er, R. Venkateswarlu, and P. Chan, "Max-mean and max-median filters for detection of small targets," *Proc. SPIE*, vol. 3809, pp. 74–84, Oct. 1999.
- [16] Y. Gu, C. Wang, B. Liu, and Y. Zhang, "A kernel-based nonparametric regression method for clutter removal in infrared small-target detection applications," *IEEE Geosci. Remote Sens. Lett.*, vol. 7, no. 3, pp. 469–473, Jul. 2010.
- [17] H. Deng, X. Sun, M. Liu, C. Ye, and X. Zhou, "Small infrared target detection based on weighted local difference measure," *IEEE Trans. Geosci. Remote Sens.*, vol. 54, no. 7, pp. 4204–4214, Jul. 2016.
- [18] X. Bai and Y. Bi, "Derivative entropy-based contrast measure for infrared small-target detection," *IEEE Trans. Geosci. Remote Sens.*, vol. 56, no. 4, pp. 2452–2466, Apr. 2018.
- [19] Y. Li, Y. Zhang, J.-G. Yu, Y. Tan, J. Tian, and J. Ma, "A novel spatio-temporal saliency approach for robust dim moving target detection from airborne infrared image sequences," *Inf. Sci.*, vol. 369, pp. 548–563, 2016.
- [20] S. Qi, J. Ma, C. Tao, C. Yang, and J. Tian, "A robust directional saliency-based method for infrared small-target detection under various complex backgrounds," *IEEE Geosci. Remote Sens. Lett.*, vol. 10, no. 3, pp. 495–499, May 2013.
- [21] Y. Wei, X. You, and H. Li, "Multiscale patch-based contrast measure for small infrared target detection," *Pattern Recognit.*, vol. 58, pp. 216–226, Oct. 2016.
- [22] H. Deng, X. Sun, and X. Zhou, "A multiscale fuzzy metric for detecting small infrared targets against chaotic cloudy/sea-sky backgrounds," *IEEE Trans. Cybern.*, vol. 49, no. 5, pp. 1694–1707, May 2019.
- [23] P. Chiranjeevi and S. Sengupta, "Detection of moving objects using multi-channel kernel fuzzy Corelogram based background subtraction," *IEEE Trans. Cybern.*, vol. 44, no. 6, pp. 870–881, Jun. 2014.
- [24] X. Bai, Z. Chen, Y. Zhang, Z. Liu, and Y. Lu, "Infrared ship target segmentation based on spatial information improved FCM," *IEEE Trans. Cybern.*, vol. 46, no. 12, pp. 3259–3271, Dec. 2016.
- [25] B. Recht, M. Fazel, and P. A. Parrilo, "Guaranteed minimum-rank solutions of linear matrix equations via nuclear norm minimization," *SIAM Rev.*, vol. 52, no. 3, pp. 471–501, 2010.
- [26] E. J. Candès, X. Li, Y. Ma, and J. Wright, "Robust principal component analysis?" *J. ACM*, vol. 58, no. 1, pp. 1–37, 2009.
- [27] F. Nie, H. Huang, and C. Ding, "Low-rank matrix recovery via efficient Schatten p -norm minimization," in *Proc. 26th AAAI Conf. Artif. Intell.*, vol. 1, 2012, pp. 655–661.
- [28] Y. Xie, S. Gu, Y. Liu, W. Zuo, W. Zhang, and L. Zhang, "Weighted Schatten p -norm minimization for image denoising and background subtraction," *IEEE Trans. Image Process.*, vol. 25, no. 10, pp. 4842–4857, Oct. 2016.
- [29] W. Wang, V. Aggarwal, and S. Aeron, "Tensor completion by alternating minimization under the tensor train (TT) model," 2016, *arXiv:1609.05587*. [Online]. Available: <https://arxiv.org/abs/1609.05587>
- [30] G. Xu, S. Khan, H. Zhu, L. Han, M. K. Ng, and H. Yan, "Discriminative tracking via supervised tensor learning," *Neurocomputing*, vol. 315, pp. 33–47, Nov. 2018.
- [31] X. Wang, L. T. Yang, L. Kuang, X. Liu, Q. Zhang, and M. J. Deen, "A tensor-based big-data-driven routing recommendation approach for heterogeneous networks," *IEEE Netw.*, vol. 33, no. 1, pp. 64–69, Jan./Feb. 2019.
- [32] L. Deng, H. Zhu, Y. Li, and Z. Yang, "A low-rank tensor model for hyperspectral image sparse noise removal," *IEEE Access*, vol. 6, pp. 62120–62127, 2018.
- [33] J. Serra, *Image Analysis and Mathematical Morphology*. New York, NY, USA: Academic, 1982.
- [34] B. Ye and J. X. Peng, "Small target detection method based on morphological top-hat operator," (in Chinese), *J. Image Graph.*, vol. 7, pp. 15–19, 2002.
- [35] X. Bai, F. Zhou, and Y. Xie, "New class of top-hat transformation to enhance infrared small targets," *Proc. SPIE*, vol. 17, no. 3, 2008, Art. no. 030501.
- [36] X. Bai and F. Zhou, "Analysis of new top-hat transformation and the application for infrared dim small target detection," *Pattern Recognit.*, vol. 43, no. 6, pp. 2145–2156, 2010.
- [37] J. Mira, A. E. Delgado, A. Fernández-Caballero, and M. A. Fernández, "Knowledge modelling for the motion detection task: The algorithmic lateral inhibition method," *Expert Syst. Appl.*, vol. 27, no. 2, pp. 169–185, 2004.
- [38] Y. Won, P. D. Gader, and P. C. Coffield, "Morphological shared-weight networks with applications to automatic target recognition," *IEEE Trans. Neural Netw.*, vol. 8, no. 5, pp. 1195–1203, Sep. 1997.
- [39] S. Yang, J. Wang, W. Fan, X. Zhang, P. Wonka, and J. Ye, "An efficient ADMM algorithm for multidimensional anisotropic total variation regularization problems," in *Proc. ACM SIGKDD Int. Conf. Knowl. Discovery Data Mining*, 2013, pp. 641–649.
- [40] P. Purkait and B. Chanda, "Super resolution image reconstruction through Bregman iteration using morphologic regularization," *IEEE Trans. Image Process.*, vol. 21, no. 9, pp. 4029–4039, Sep. 2012.



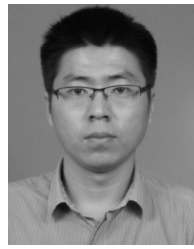
Hu Zhu (M'17) received the B.S. degree in mathematics and applied mathematics from the Huaibei Coal Industry Teachers College, Huaibei, China, in 2007, and the M.S. and Ph.D. degrees in computational mathematics and pattern recognition and intelligent systems from the Huazhong University of Science and Technology, Wuhan, China, in 2009 and 2013, respectively.

In 2013, he joined the Nanjing University of Posts and Telecommunications, Nanjing, China. His research interests include pattern recognition, image processing, and computer vision.



Shiming Liu received the B.S. degree in communication engineering from Henan Polytechnic University, Jiaozuo, China, in 2017. He is currently pursuing the master's degree in electronics and communication with the Nanjing University of Posts and Telecommunications, Nanjing, China.

His research interest includes computer vision.



Yansheng Li received the B.S. degree in information and computing science from Shandong University, Weihai, China, in 2010, and the Ph.D. degree in pattern recognition and intelligent system from the Huazhong University of Science and Technology, Wuhan, China, in 2015.

He was an Assistant Professor with Wuhan University (WHU), Wuhan, China, in 2015, and became an Associate Research Fellow in 2017, where he is currently an Associate Professor with the School of Remote Sensing and Information Engineering. From 2017 to 2018, he was a Visiting Assistant Professor with the Department of Computer Science, Johns Hopkins University, Baltimore, MD, USA. He has authored more than 30 peer-reviewed articles (SCI papers) in international journals from multiple domains, such as remote sensing and computer vision. His research interests include computer vision, machine learning, and their applications in remote sensing big data analysis.



Lizhen Deng (M'17) received the B.S. degree in electronic information science and technology from the Huaibei Coal Industry Teachers College, Huaibei, China, in 2007, and the M.S. degree in communication and information systems from the Nanjing University of Aeronautics and Astronautics, Nanjing, China, in 2010, and the Ph.D. degree in electrical engineering from the Huazhong University of Science and Technology, Wuhan, China, in 2014.

In 2014, she joined the Nanjing University of Posts and Telecommunications, Nanjing. Her research interests include image processing, computer vision, pattern recognition, and spectral data processing.



Fu Xiao (M'12) received the Ph.D. degree in computer science and technology from the Nanjing University of Science and Technology, Nanjing, China, in 2007.

He is currently a Professor and a Ph.D. supervisor with the School of Computer, Nanjing University of Posts and Telecommunications, Nanjing. He has authored papers in related international conferences and journals, including INFOCOM, the IEEE International Conference on Communications (ICC), the IEEE International Performance, Computing and Communications Conference (IPCCC), the IEEE JOURNAL ON SELECTED AREAS IN COMMUNICATIONS, the IEEE/ACM TRANSACTIONS ON NETWORKING, the IEEE TRANSACTIONS ON MOBILE COMPUTING, the *ACM Transactions on Embedded Computing Systems*, and the IEEE TRANSACTIONS ON VEHICULAR TECHNOLOGY. His research interest includes Internet of Things.

Dr. Xiao is a member of the IEEE Computer Society and the Association for Computing Machinery.